Contents lists available at ScienceDirect

Materials Science & Engineering B

Effect of thermal treatment on the 4f-hopping conductivity of CeO_2 exposed to $CO_{(g)}$ atmosphere

Alley Michael da Silva Procópio [a,*], Leandro Silva Rosa Rocha [d], Paula Mariela Desimone [b], Giuliana Giulietti [b], Celso Manuel Aldao [c], Elson Longo [d], Francisco Moura [a], Miguel Adolfo Ponce [a,b]

[a] *Advanced Materials Interdisciplinary Laboratory (LIMAv), Federal University of Itajubá – Campus Itabira, 200, Industrial District II, 35.903-087, MG, Brazil*
[b] *Institute of Materials Science and Technology (INTEMA), University of Mar del Plata and National Council of Scientific and Technical Research (CONICET), Av. Colón 10850, B7606FWV Mar del Plata, Argentina*
[c] *Institute of Scientific and Technological Research in Electronics (ICYTE), University of Mar del Plata and National Council of Scientific and Technical Research (CONICET), Juan B. Justo 4302, B7608FDQ Mar del Plata, Argentina*
[d] *Center for Research and Development of Functional Materials (CDMF), Federal University of São Carlos (UFSCar), São Carlos, Brazil*

ARTICLE INFO

ABSTRACT

The thermal treatment of CeO_2 at 600 and 900 °C on the film response against CO is analyzed. A fluorite-type crystalline structure was observed, with the later presenting a well-defined morphology formed by the set of $(1\,0\,0)$, $(1\,1\,0)$ and $(1\,1\,1)$ surfaces. The band-gap was 3.35 and 3.37 eV, for the 600 and 900 °C samples. We have proposed an equation based on the mass action law that shows the dependence of the carriers density as a function of the grain size, demonstrating that the area-volume relation can affect the number of charge carriers, which reflects in the pre-exponential A factor of conductivity. Reducing gases generate a greater number of carriers available for conduction, reflected on the A factor. When vacancies are annihilated by exposing to an oxygen atmosphere, the Ce (III) amount reduces. The activation energy and pre-factor A in air, vacuum and CO were calculated for correlating with the sample morphologies.

1. Introduction

Cerium oxide, CeO_2, is a widely used oxide due to its interesting characteristics such as the mobility of oxygen in the crystal lattice and the lack of intrinsic stoichiometry [1,2]. CeO_2 is an *n*-type semiconductor, with a band-gap of 3.44 eV (O2p-Ce4f transitions) and a fluorite-like cubic structure. The proposed electrical transport mechanism is characterized by the hopping of electrons in a cluster-to-cluster charge transfer (CCCT) process [3].

Cerium oxide is currently used in catalysis and systems for the purification of gaseous emissions in automobiles, solid state fuel cells, as well as a gas sensor [4,5]. The sensors' properties of CeO_2 *versus* carbon monoxide (CO) have been extensively studied [6-9], with Izu et al. showing that CeO_2 has a better sensory response to CO than SnO_2. It is known that in the presence of CO, the electrical resistance of CeO_2 decreases due to an increase in the number of oxygen vacancies in the material, accompanied by the reduction of Ce(IV) to Ce(III) [10].

Our group has extensively studied the preparation, properties, and applications of pure and doped ceria nanostructures over the last few years. Ultimately, Ortega et. al.[9] studied rare-earth doped CeO_2 nanostructures obtained by the microwave-assisted hydrothermal (MAH) route, showing a lattice expansion when modified with La and Eu, with oxygen vacancies as the dominant defect, besides a response time of only 1 s, for the Eu-doped sample towards CO detection, along with a dual sensing behavior (electrical and optical capability) [11,12]. On top of that, Oliveira et al. [13] proposed the Ostwald ripening along with an oriented attachment as the dominant growth mechanism for the ceria nanostructures, observing an evolution from sheet to cube-like morphologies with an increasing synthesis time, while Amoresi et al. [14] showed that distinct morphologies such as rods, beans, hexagons and cubes could be obtained by changing the mineralizer concentration and evaluated their photo-catalytic activity towards ciprofloxacin degradation, with distinct functional groups being attacked depending on the morphology, owing to a combination of specific exposed

crystalline facets and surface defects. Additionally, Fan, Z. et al. [15] studied flower-like CeO2/TiO2 heterostructures for photocatalytic degradation of Rhodamine B (RhB) under UV light irradiation, showing that flower-like heterostructures exhibited markedly enhanced photocatalytic activity compared with pure CeO2, pure TiO2 and commercial P25, attributing the enhanced photocatalytic activity to the improvement of charge separation derived from the coupling effect of TiO2 and CeO2 heterostructures.

In this way, we were able to display the materials' properties dependence upon their structure and morphology, showing that heat treatments could be an effective strategy to induce crystallization of distinct morphologies accompanied by different properties, not to mention other distinct oxides with the same behavior reported in literature [16,17].

In regards to the electronic properties of ceria-based nanomaterials, the small polaron theory along with the hopping conduction mechanism [18] shows a predominance in controlling the phenomena, with the charge conduction process locally controlled by the so-called cluster-to-cluster charge transfer (CCCT) mechanism, with a probability that roughly depends on the distance between adjacent species [10]. Additionally, Blumenthal, R.N. et al. [19,20] showed that the hopping-type conductivity occurs in reduced (CeO_{2-x}) ceria-based systems with a hopping activation energy (Ea) of 0.22 eV at a low x, which increased with an increasing x.

In this work, thermal treatments (TT) at 600 and 900 °C were carried out to investigate its influence on the grain size and on the electrical behavior of pure CeO2, when exposed to distinct gaseous atmospheres, with particular attention given to the hopping conduction mechanism under reductive atmospheres.

2. Experimental section

CeO2 nanoparticles were synthesized through the polymeric precursors' method (PPM), using a stoichiometric ratio of 1 mol Ce (NO3)3·6H2O: 4 mol citric acid: 16 mol ethylene glycol. A citric acid aqueous solution was added to the Ce(NO3)3·6H2O aqueous solution for Ce metal complexation process, which remained for 30 min under stirring, at 60 °C. The pH of the resulting solution was adjusted to 6. For the polyesterification reaction, ethylene glycol was added to the previous solution, under stirring, at 50 °C, for 12 h. 400.00 mL of a Ce polymeric resin was kept under stirring for three weeks, at 110 °C. Subsequently, the obtained material was heated to 300 °C with a heating rate of 5 °C. min^{-1} for 120 min. Then, the CeO2 agglomerates were macerated and sieved on a 53 μm sieve (270 mesh). In alumina crucibles, CeO2 powder was heat treated at 600 and 900 °C with a heating rate of 5 °C.min^{-1} for 120 min.

For the characterization of CeO2 powders, X-Rays diffraction (XRD), Raman Spectroscopy, Ultraviolet–Visible (UV-Vis) Optical Spectroscopy and Scanning Electron Microscopy (SEM) were used. For the XRD analysis, a diffractometer was used, with a copper tube (Cu-Ka, k = 1.5406 Å), at 40 kV and 60 mA. Diffraction spectra were obtained in the range of 2γ, between 20 and 80°, in continuous mode, at 0.02°.s^{-1}. The Raman spectrometer consists of a Senterra model (Bruker), coupled to an optical microscope and equipped with a He-Ne laser (λ = 633 nm) at a power of 5.00mW, with a CCD detector (Charge-Coupled Device) submitted to a resolution of 3–5 cm^{-1} in a spectral region from 40 cm^{-1} to 3530 cm^{-1}, using a 100x objective and 50 × 1000 μm lens aperture. The UV–Vis measurements were performed in a spectrophotometer model UV-2600 (Shimadzu) in diffuse reflectance mode, in a spectral region of 185 nm to 1400 nm. The scanning electron microscopy images were obtained with a FEG-SEM Supra 35-VP equipment using 5 kV of accelerating voltage.

For the gas-sensing measurements, an alumina wafer was used as a substrate, with an adhesion layer of 25 nm of titanium deposited on it, below a 200 nm-thick platinum film used as the electrode, both produced by RF-sputtering. The interdigitated electrodes were imprinted by

laser (λ = 355 nm, v = 2KHz with a pace of 2 mm/s), with a spacing of 50 μm. Thick and porous films were prepared on top of the resulting substrates by a screen-printing-like method, previously described in literature [11], and then kept in a laboratory oven at 100 °C for 24 h, in air, for glycerol evaporation and improved adhesion of the films to the alumina substrate. Afterwards, the samples were thermally treated at 380 °C for 1 h in air atmosphere, and then the gas-sensing measurements were finally carried out. The measurements were made in an optoelectronic device for the characterization of materials, with intellectual properties deposition in Brazil (BR1020160283833) and Argentina (AR2015P103953), under temperature and pressure control. The electrical resistance was measured with an Agilent 3440A multimeter.

3. Results and discussion

3.1. Powders characterization

3.1.1. XRD measurements

To identify the phase and crystalline structure of the powders after the heat treatment at 600 and 900 °C, the XRD technique was used. The analysis of Fig. 1 reveals that the XRD patterns for both samples correspond to the (111), (200), (220), (311), (222), (400), (331), (420), (422), (511), and (440) plane reflections of CeO2, as denoted by the International Center for Diffraction Data (JCPDS 34-394) [21], well indexed to the fluorite-type crystalline structure of CeO2 which confirms the pure phase of the material without secondary phases. The fluorite crystal structure of CeO2 presents a cubic structure with space group $Fm\overline{3}m$ and has one unit formula per primitive cell, where each Ce atom is coordinated by eight O atoms, forming [CeO8] clusters [8].

This result shows the efficiency and success of the synthesis method used. It is also possible to affirm that the temperature has an important role in the long-range order of the samples, as observed by the narrowing of the peak widths for the sample calcined at 900 °C [22].

Additionally, the average crystallite size was determined using the Debye-Scherrer formula, seen in Equation (1).

$$t = \frac{0.9 \times \lambda}{B \times cos(\theta_B)} \tag{1}$$

Where t corresponds to the CeO2 average crystallite size, λ, the wavelength of the used radiation (Co = 1.7899 Å), B is the full width at half maximum (FWHM) parameter, measured in radians, and θ_B the angular value of the high-intensity diffraction line shown in Fig. 1. The obtained crystallite sizes were 17.21 and 41.69 nm (peak position of 27.88 and 27.82°, and FWHM of 0.57705 and 0.23812°, respectively)
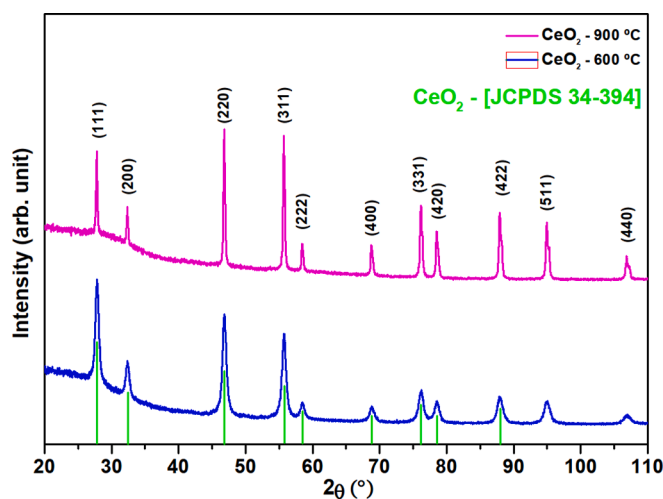

Fig. 1. XRD patterns for the CeO2 powders with heat treatment at 600 and 900 °C.

for the samples calcined at 600 °C and 900 °C, respectively. These values are in good agreement with the ones calculated for the nanofibers of CeO₂ obtained by electrospinning with post-synthesis calcination at 500, 600, 700, and 800 °C, with crystallite sizes of 13, 16, 23 and 46 nm [23], respectively, accompanied by the narrowing of the diffraction peaks with the increasing calcination temperature. Besides, Arabaci, A. [24] prepared cerium oxide obtained by the Pechini method and calcined at 400 and 500 °C, with crystallite sizes of 11 and 13 nm. Additionally, Carregosa, J.D.C. et al. [25] obtained average crystallite sizes of 18.1 and 18.5 nm for a calcination at 700 °C, whilst the uncalcined samples showed values of 6.90 and 7.15 nm, after synthesized by the microwave assisted hydrothermal (MAH) route, corroborating the strong influence of the heat treatment on the microstructural properties of ceria-based nanostructures.

3.1.2. Microstructural characterization

SEM analyses were carried out in order to observe the type of morphology of the CeO₂ samples treated at different temperatures. From the SEM images in Fig. 2A and B, it is possible to observe that the samples have shown a compact aspect with undefined morphologies for the one calcined at 600 °C and that the one calcined at 900 °C depicted fractals of a cuboctahedral morphology with distinct sizes. According to literature [26], from theoretical calculations, the (1 1 1) surface is the most stable surface of the CeO₂, with the lower surface energy (E_{surf}) value. Therefore, the ideal morphology of the CeO₂ would only show the (1 1 1) exposed surfaces. In this regard, using an Ab initio strategy developed by Andres et al. [27] with the association of the E_{surf} values and the Wulff theorem, it is possible to simulate the experimental morphologies of any material. In this way, to generate the morphology of the CeO₂ at 900 °C, it is necessary to decrease the E_{surf} value of the (1 0 0) and (1 1 0) surfaces [26]. Therefore, it is possible to assume that the heat treatment at 900 °C caused the stabilization of the (1 0 0) and (1 1 0) facets, forming this well-defined morphology serving as a driving force for the CeO₂ growth process. The improvement of the crystalline microstructure would likely lead to a higher charge carrier concentration.

Regarding the change of morphology owing to changes in the synthesis parameters, Meng, F., Wang, L., Cui, J. [28] showed that the increase of ethanol/water ratio resulted in the morphology change from thin nanorods to short-thick nanorods, and then to nanoparticles in nano-CeO₂ systems, obtained by a facile hydrothermal route, attributing these changes to the influences of hydrocarbon chains, dielectric constant, and viscosity of the solution on the thermodynamics of the reaction system and kinetics of nucleation.

In regards to the grain sizes, the sample treated at 600 °C had relatively smaller grains compared to the one calcined at 900 °C, besides undefined morphology, as seen in Fig. 2. According to the literature, it is known that calcination rises the amount of oxygen vacancies depending on the calcination atmosphere and temperature [29,30]. However, some authors propose a reduction of the number of oxygen vacancies when increasing the calcination temperature [31] likely related to the possible in-diffusion of oxygen species towards the bulk of the material. Therefore we have a delicate balance between the amount of defective species on the surface and on the bulk, besides the contribution of local charge transfer processes that could influence the response towards carbon monoxide detection.

3.1.3. Raman spectroscopy analysis

The short-range order–disorder of the CeO₂ nanoparticles was investigated using Raman spectroscopy technique, for the evaluation and identification of the normal vibration modes of CeO₂. The CeO₂ crystallizes in a fluorite-like cubic structure belonging to space group $Fm\overline{3}m$ and this structure, has only one active Raman mode near 465 cm^{-1}. This mode is associated with the triply degenerate F_{2g} symmetric stretching of Ce–O bonds in the $[CeO_8]$ clusters [32]. As illustrated in Fig. 3, this characteristic mode appears in both samples (600 and 900 °C), confirming the fluorite-type phase formation, in accordance with the XRD results. Despite the arbitrary units, we can perceive the higher intensity of the peak for the sample calcined at 900 °C, which indicates a higher degree of short-range order [33] for this sample, which goes along with the presence of well-defined morphologies, as seen in Fig. 2.

For comparison purposes, it is also possible to estimate the average crystallite sizes from the Raman broadening [34], using a simple equation of β (cm^{-1}) = 10 + (124.7/D), where β corresponds to the full width at half maximum (FWHM) of the Raman active mode and D, the particle size. This estimation provided values of 33.70 and 69.27 nm, for the samples calcined at 600 and 900 °C respectively, which were slightly higher than the values obtained by the XRD estimation, although corroborating the increasing grain size with the higher calcination temperature.

3.1.4. UV–Vis measurements

In order to determine the effective band gap energy (E_{gap}) of the samples, diffuse reflectance spectroscopy of UV–Vis spectra was carried out based on the theories of Kubelka-Munk (K-M) and mathematical models of Wood-Tauc (W-T) [35], as shown in Fig. 4.

In general, The E_{gap} of semiconductor oxides is related to the electronic transition between the valence (VB) and conduction bands (CB). In our case, the electron transitions occur between VB and Ce-4f states and can also be calculated by Equation (2) of W-T [36]:
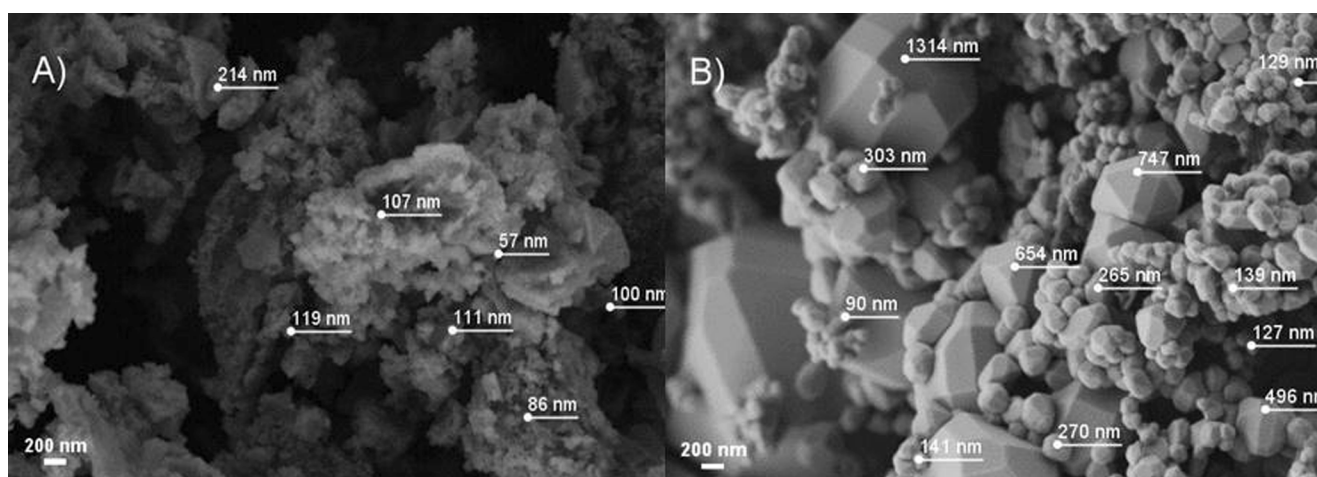

Fig. 2. Scanning electron microscopy of the particles after calcination at (A) 600 and (B) 900 °C.
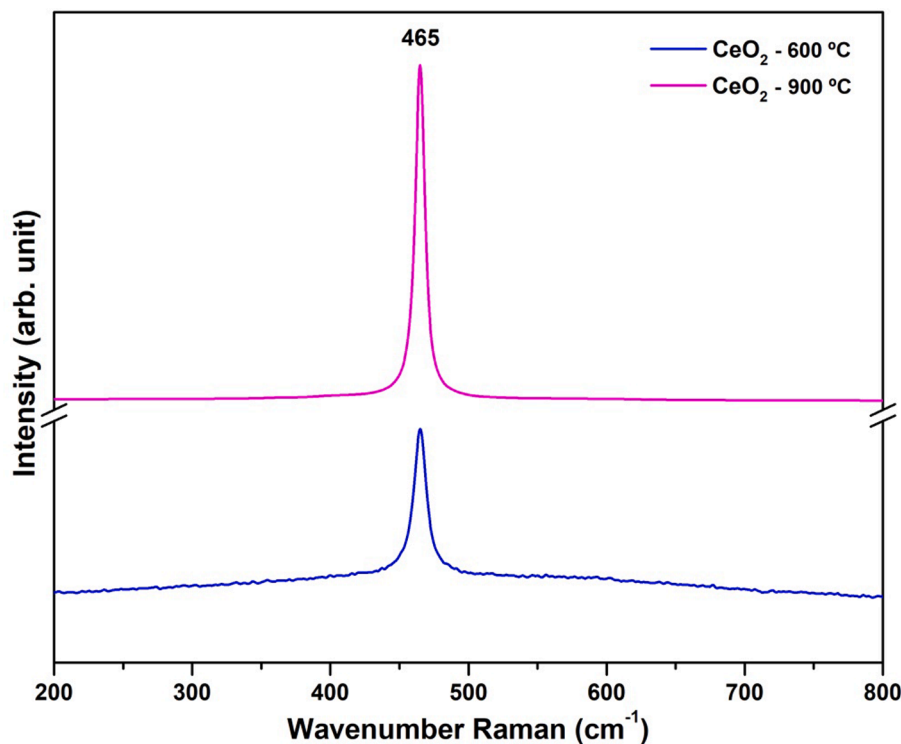
Fig. 3. Raman spectroscopy of the particles prepared by the PPM with post-synthesis calcination at distinct temperatures.
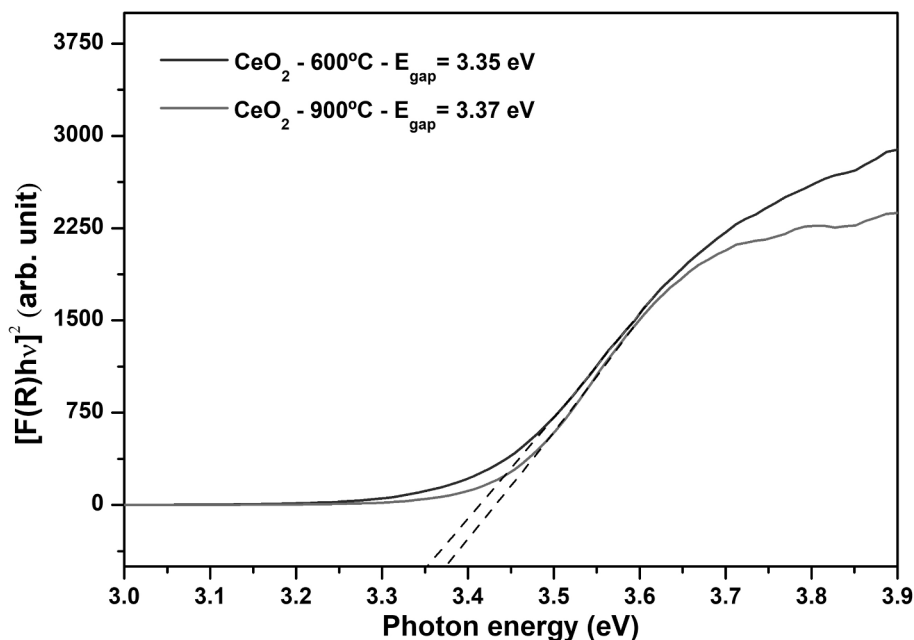

Fig. 4. UV–Vis measurements of the particles' effective band-gap.

$$\alpha h\nu = A\left(h\nu - E_{gap}\right)^{n} \tag{2}$$

where, α is absorption coefficient, h ($6{,}6262 \times 10^{-34}$ J s) is Planck's constant, A is absorption constant, ν (s^{-1}) is frequency, E_{gap} (eV) is band gap energy, n is the variable that depends on the type of possible electronic transitions between the VB and CB, and can take on values of 2 for an indirect allowed transition, 3 for an indirect forbidden, 1/2 for a direct allowed and 3/2 for a direct forbidden.

Then, for K-M and W-T theories, we have the following Equation (3) [37]:

$$\left[F(R)h\nu\right]^{1/n} = A\left(h\nu - E_{gap}\right) \tag{3}$$

To determine the E_{gap} value, we plot $\left[F(R)h\nu\right]^{1/n}$ as a function of the photon energy (hν), as shown in Fig. 4. The E_{gap} is determined by extrapolating the linear portion of the graph to $\left[F(R)h\nu\right]^{1/n} = 0$. Then, from UV–Vis measurements, we can conclude that the sample with higher crystallinity, treated at 900 °C, showed a mild increase of the band gap measured as "E_{gap}" compared to the sample with minor crystallinity, treated at 600 °C, from 3.35 to 3.37 eV, or to say a change of

4

only 0.02 eV. This behavior goes along with the higher degree of organization, seen in the sample calcined at 900 °C, in accordance with the XRD, SEM and Raman measurements, giving rise to a higher band gap value, also seen in the literature for nickel oxide [38], as well as for cerium oxide nanoparticles [39], despite the possible generation of local oxygen vacancies as a consequence of the higher calcination temperature. In this way, we can say that the number of defects, the particular electronic configuration of its constituents and the dominant morphologies play the major role when it comes to the electrical charge transfer

mechanism in nanostructured semiconductor materials.

According to literature, it is also possible to alter the band gap values for ceria-based nanomaterials changing its synthesis time, as reported by Wang, L. *et al.* [40], resulting in an effective red shifting of the band gap, from 3.014, 3.099, 2.931, to 2.927 eV by increasing the hydrothermal synthesis time within 2, 18, 50, and 100 h, respectively.
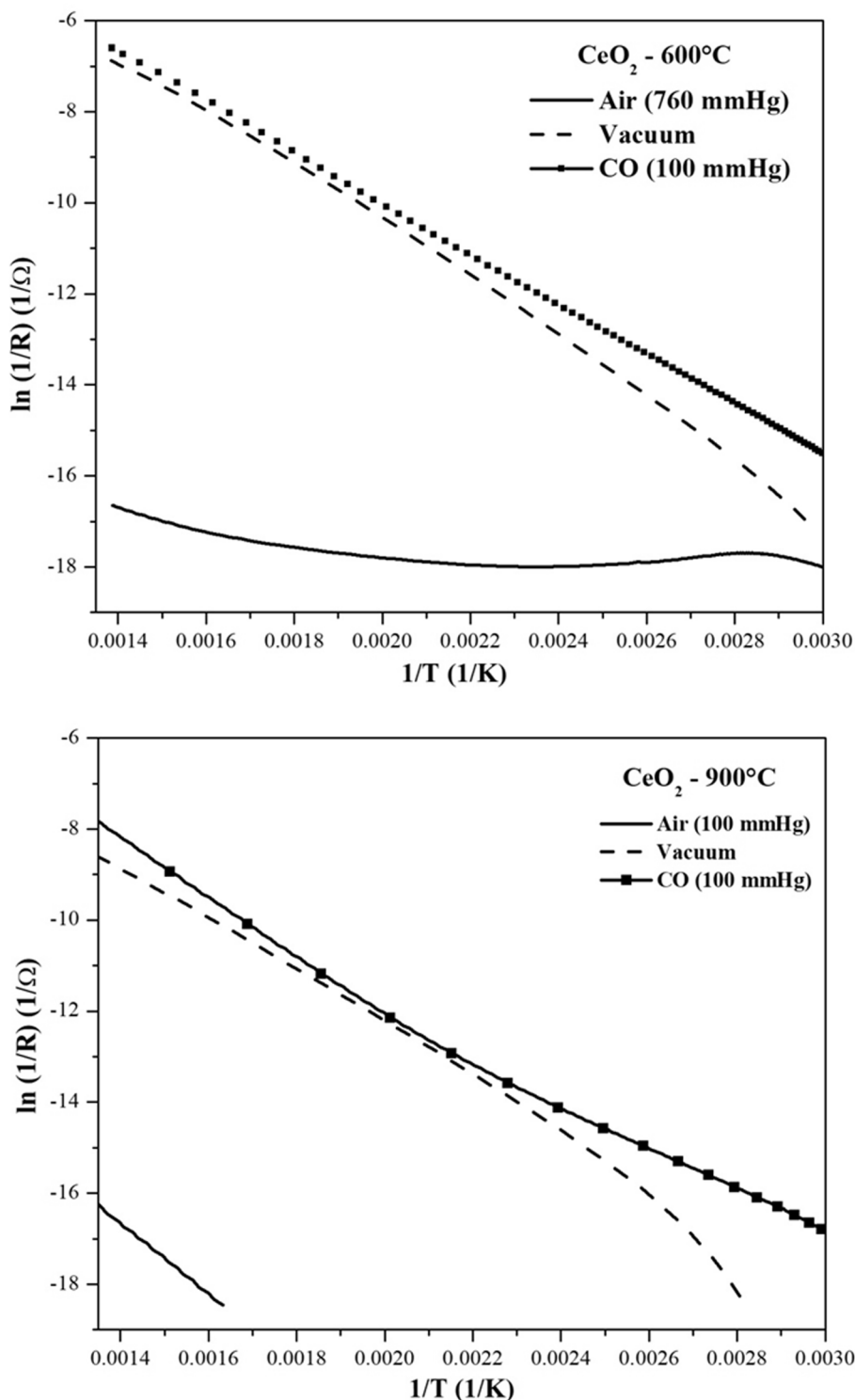

Fig. 5. Resistance *vs* Temperature measurements for the samples calcined at distinct temperatures.

3.2. Films characterization

3.2.1. Electrical behavior

Fig. 5 shows the cooling of three temperature cycles that were carried out in presence of air, vacuum and carbon monoxide in order to study the films electronic activation energies for the hopping conduction mechanism.

Table 1 shows the Electronic Activation Energy (Ea$_e$) values obtained from Fig. 5A and B, with their respective pre-exponential factors (A). The values of the Ea$_e$ in air, vacuum and CO were calculated applying the Equation (4) for the hopping conduction mechanisms.

$$G = (A/T)exp^{\frac{-Ea_e}{kT}} \tag{4}$$

where G corresponds to the hopping conductivity, A the exponential factor that depends on the carrier concentration, E_{ae} the electronic activation energy, k the Boltzmann's constant, and T the temperature in Kelvin.

Thus, the electrical conductivity depends on the activation energy and on the number of carriers (electrons) available for conduction, which is directly related to the pre-exponential value of A. In Table 1 it can be seen that A increases when the material is exposed to the following sequence of atmospheres: air, vacuum and CO [41]. Since the electrical conduction takes place through hopping between 4f levels of Ce, the number of electrons involved in conduction is governed by the occupation of these states. This is governed by the position of the Fermi level, which can be determined by resorting to electrical neutrality.

Involved charges mainly include ionized oxygen vacancies at the bulk of the grains, ionized acceptor levels due to adsorbed oxygen at the surface of the grains, and electrons at the 4f levels. In the absence of adsorbed oxygen (flat band condition), negative charge due to electrons at the 4f levels must be equal to the positive charge due to ionized vacancies. This means that the density of electrons n must be equal to twice the density of oxygen vacancies V and then, assuming all are ionized, $n = 2[V]$. In this case, the conductivity would only depend on the density of oxygen vacancies.

Regularly, oxygen adsorption is described according to **Equation (5)** [42]:

$$O_2 + 2\alpha e = 2O^{\alpha-} \tag{5}$$

where α can be 1 or 2 depending on the ionization of adsorbed oxygen, singly or doubly charged, respectively. Then, by applying the mass action law, we reach on **Equation (6)**:

$$n^{2\alpha} p_{O_2} \propto \sigma_s^2 \tag{6}$$

where γ_s is the surface charge density due to adsorbed oxygen, P_{O2} is the partial pressure of oxygen and n is the carriers density. For a high oxygen pressure, we can expect that most electrons originated in ionized oxygen vacancies end at ionized acceptors located at the surface of the grains. Thus, for a spherical grain, we have **Equation (7)**:

$$\frac{4}{3}\pi r^3 [V] \propto 4\pi r^2 \sigma_s \tag{7}$$

where r is the grain radius. Finally, with **Equations (6) and (7)**, we can write **Equation (8)**:

$$n \propto \frac{([V]r)^{1/\alpha}}{p_{O_2}^{1/2\alpha}} \tag{8}$$

Equation (8) explicitly shows the dependence of the carriers density as a function of the grain size. Then, we expect that under a high oxygen pressure, being the other relevant parameters constant, the conductivity would decrease with the grain size of our samples. However, samples calcined at 900 °C present a much lower conductivity as we had to reduce the air pressure to 100 mmHg to be able to carry out resistance measurements, despite the larger grains seen in Fig. 2. This indicates that the reduced conductivity is related to the lower amount of oxygen vacancies.

On the other hand, the larger conductivity under vacuum or CO, of the sample treated at 600 °C is simpler to rationalize. Due to the reduction of oxygen at the surface, films with smaller grains are more affected as their ratio surface/volume is larger, and therefore a larger conductivity is expected. Specially, this can be easily observed in Fig. 6A and B.

Considering the activation energy (E_{ae}) for the two samples among the three distinct atmospheres, we can see that the one treated at 900 °C presented higher values, which goes along with the suggestion that the larger the grains, the more energy is required for the electrons to hop from one level to the neighboring one.

To gather more information regarding the electrical behavior, the response was measured as a function of time as shown in Fig. 6, enabling the determination of the response time (t$_{resp}$) for the carbon monoxide atmosphere. As shown, the electrical resistance was measured in cycles of air, vacuum and carbon monoxide for 10 min on each atmosphere, under 380 °C. The selected temperature corresponds to the so-called working temperature, where CO promptly reacts with net surface oxygen as shown in previous works [9,10,12,13], and the samples' resistance can be easily measured with our instruments.

When the thermal treatment temperature is increased, the overall electrical resistance is higher, which can be associated with the decrease in the number of oxygen vacancies as a consequence of their annihilation due to the oxygen in-diffusion [8,11-13].

In our experimental conditions, in which the samples are exposed to vacuum, air and CO atmospheres, a great variation in the carrier concentration occurs. Oxidant atmosphere (air) decreases the carrier concentration and a rapid decrease in the conductivity is observed in Fig. 6A and B. Vacuum or reducing atmospheres, otherwise, increase the carrier concentration and a rapid increase of the conductivity is perceived. The observed behavior in Fig. 6 is consistent with the pre-exponential factors of Table 1 and are also consistent with previously reported values for CeO$_2$ polycrystalline semiconductors [41].

The gaseous atmosphere was changed and response times were calculated in Table 2.

Despite the higher activation energies (Table 1) required for the electrons to hop on the sample calcined at 900 °C, owing to the larger grains, the response times for detecting the carbon monoxide atmosphere were lower for both pressure conditions (10 and 50 mmHg), reducing from 19 to 4 s, and from 12 to 3 s, strongly suggesting that the electrons transfer phenomena is locally controlled by a delicate balance between defective species, such as oxygen vacancies and Ce(III) ions on the forbidden gap, the morphologies, and the crystalline facets exposed to the interaction with the gas.

Besides the electrical response that ceria-based nanomaterials present, they can also exhibit room temperature ferromagnetism, with the saturation magnetization (Ms) gradually increasing with the increase on the band gap, as reported by Wang, L. and Meng, F. [43], with the highest Ms of 0.167 emu/g obtained for CeO$_2$ nanopoles synthesized within 100 h, depicting its multifuncionality towards several applications.

4. Conclusion

In this work we have demonstrated that an increase of the defects is reflected as an energy widening of the cerium 4f states distribution and this can change the film conductance behaviors. Moreover, the cerium 4f
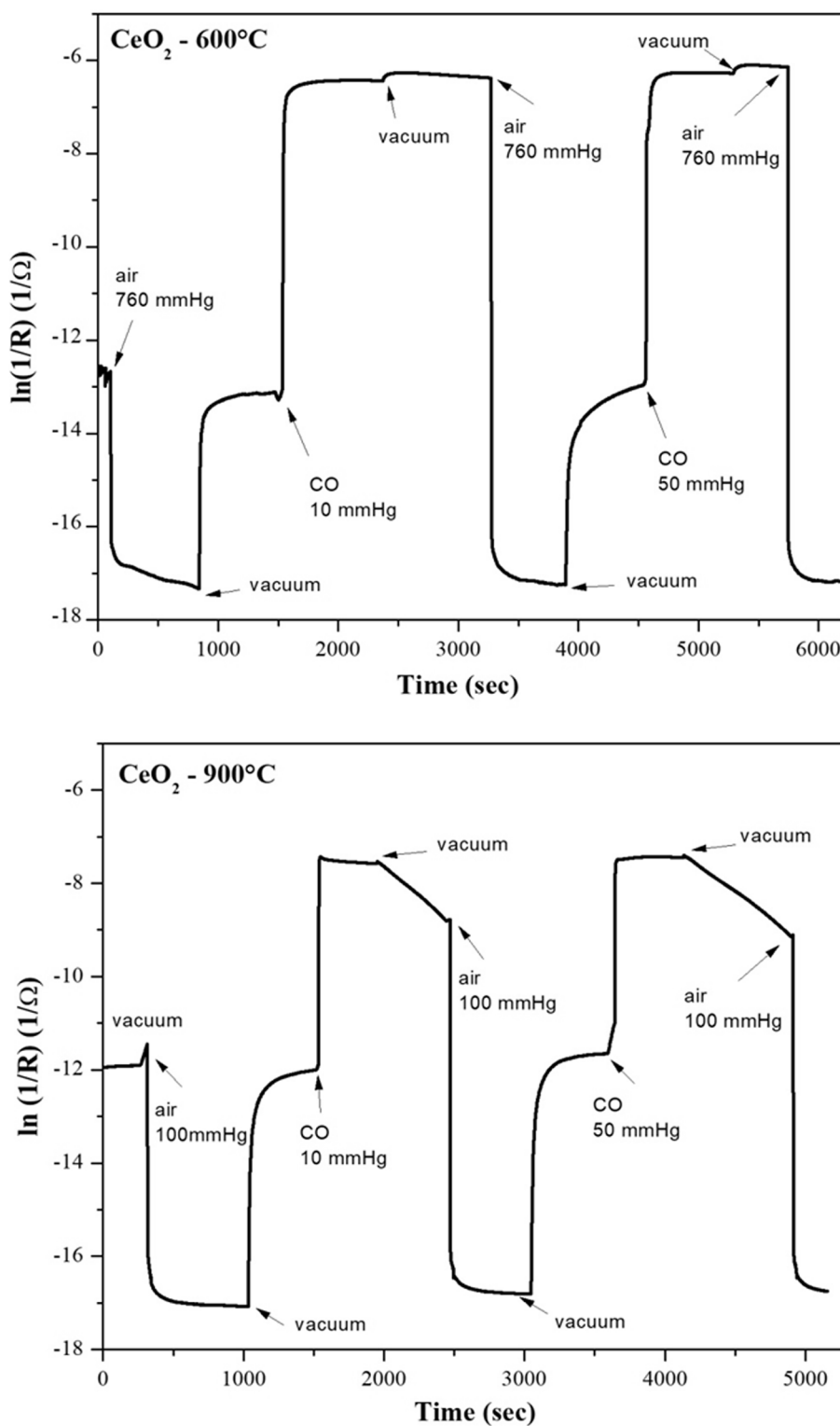
Table 1
Obtained values of A (a.u) and E_{ae} (eV) for both TT (°C) in air, vacuum and CO.

Atm	Air		Vacuum		CO	
TT	A	E_{ae}	A	E_{ae}	A	E_{ae}
600	0.093	0.44	1261	0.46	5432	0.54
900	167	0.50	565	0.53	2540	0.60

Fig. 6. Resistance *vs.* Time measurements for the samples calcined at distinct temperatures.

states of samples with lower crystallinity (TT of 600 °C) appear closer to the valence band according to the UV–Vis results. This suggests that the thermal treatment at higher temperatures could cause a narrower dispersion of the possible Cerium-4f^0 states (Ce(IV)) to which electrons could jump from a Cerium-4f^1 state (Ce(III)) now deeper in energy.

It was also demonstrated that as a consequence of the grain size, the resulting area-volume relation can affect the number of charge carriers (that reflects in the pre-exponential A factor) for cerium oxide-based nanostructures. Additionally, when samples are treated with reducing gases, a greater number of carriers are available for conduction and this is also reflected on the A factor. The opposite occurs when vacancies are annihilated by exposing the samples to an oxygen atmosphere, followed by Ce (III) amount reduction.

Finally, we showed that thermal treatments can generate well-defined morphologies and this order alters the carrier concentration affecting the sample conductivity.

Table 2

Response time (t_{resp}) under carbon monoxide for the two samples calcined at different temperatures.

TT (°C)	Response time (s)	
	10 mmHg CO	50 mmHg CO
600	19	12
900	4	3

Declaration of Competing Interest

The authors declare that they have no known competing financial interests or personal relationships that could have appeared to influence the work reported in this paper.

Data availability

I have shared the link to my data in the manuscript section: DATA AVAILABILITY.

Data Availability

The raw data required to reproduce these findings are available to download from https://data.mendeley.com/datasets/6k9h97xsmn. The processed data required to reproduce these findings are available to download from https://data.mendeley.com/datasets/6k9h97xsmn.

References

[1] E.R. López-Mena, C.R. Michel, A.H. Martínez-Preciado, A. Elías-Zuñiga, Simple Route to Obtain Nanostructured CeO(2) Microspheres and CO Gas Sensing Performance, Nanoscale Res. Lett. 12 (2017) 169, https://doi.org/10.1186/s11671-017-1951-x.

[2] I.C. Fernandes Vaz, A.C. Tolentino Cabral, A.M. Silva Procópio, F.F. Moura, Films based on cerium oxide sensitive to carbon monoxide, Mater. Lett. 308 (2022), 131174, https://doi.org/10.1016/j.matlet.2021.131174.

[3] L.S.R. Rocha, R. Aparecido Ciola Amoresi, T.M. Duarte, N.L. Marana, J.R. Sambrano, C.M. Aldao, et al. Experimental and theoretical interpretation of the order/disorder clusters in CeO2:La, Appl. Surf. Sci. 2020;510. https://doi.org/10.1016/j.apsusc.2019.145216.

[4] A.C. Cabral, L.S. Cavalcante, R.C. Deus, E. Longo, A.Z. Simões, F. Moura, Photoluminescence properties of praseodymium doped cerium oxide nanocrystals, Ceram. Int. 40 (2014) 4445–4453, https://doi.org/10.1016/j.ceramint.2013.08.117.

[5] A.M.S. Procópio, J. do Carmo Lima Carvalho, T.H.R. Silveira, A.L. Valério, I.C.F. Vaz, A.C.T. Cabral, et al. CeO2 thin film supported on TiO2 porous ceramics, Mater. Lett., 2020;276:128224. https://doi.org/10.1016/j.matlet.2020.128224.

[6] N. Izu, T. Itoh, M. Nishibori, I. Matsubara, W. Shin, Effects of noble metal addition on response of ceria thick film CO sensors, Sens. Actuators B 171–172 (2012) 350–353, https://doi.org/10.1016/j.snb.2012.04.058.

[7] M.F. Al-Kuhaili, S.M.A. Durrani, I.A. Bakhtiari, Carbon monoxide gas-sensing properties of CeO2–ZnO thin films, Appl. Surf. Sci. 255 (2008) 3033–3039, https://doi.org/10.1016/j.apsusc.2008.08.058.

[8] R.C. Deus, R.A.C. Amoresi, P.M. Desimone, F. Schipani, L.S.R. Rocha, M.A. Ponce, et al., Electrical behavior of cerium dioxide films exposed to different gases atmospheres, Ceram. Int. 42 (2016) 15023–15029, https://doi.org/10.1016/j.ceramint.2016.06.151.

[9] P.P. Ortega, B. Hangai, H. Moreno, L.S.R. Rocha, M.A. Ramírez, M.A. Ponce, et al., Tuning structural, optical, and gas sensing properties of ceria-based materials by rare-earth doping, J. Alloy. Compd. 888 (2021), 161517, https://doi.org/10.1016/j.jallcom.2021.161517.

[10] L.S.R. Rocha, R.A.C. Amoresi, H. Moreno, M.A. Ramirez, M.A. Ponce, C.R. Foschini, et al., Novel Approaches of Nanoceria with Magnetic, Photoluminescent, and Gas-Sensing Properties, ACS Omega 5 (2020) 14879–14889, https://doi.org/10.1021/acsomega.9b04250.

[11] L.S.R. Rocha, M. Cilense, M.A. Ponce, C.M. Aldao, L.L. Oliveira, E. Longo, et al., Novel gas sensor with dual response under CO(g) exposure: Optical and electrical stimuli, Phys. B Condens. Matter 536 (2018) 280–288, https://doi.org/10.1016/j.physb.2017.10.083.

[12] P.P. Ortega, L.S.R. Rocha, J.A. Cortés, M.A. Ramirez, C. Buono, M.A. Ponce, et al., Towards carbon monoxide sensors based on europium doped cerium dioxide, Appl. Surf. Sci., 2019;464. https://doi.org/10.1016/j.apsusc.2018.09.142.

[13] R. Cristina de Oliveira, L. Cabral, A.C. Cabral, P.B. Almeida, N. Tibaldi, J.R. Sambrano, et al. Charge transfer in Pr-Doped cerium oxide: Experimental and theoretical investigations, Mater. Chem. Phys. 2020;249. https://doi.org/10.1016/j.matchemphys.2020.122967.

[14] R.A.C. Amoresi, R.C. Oliveira, N.L. Marana, P.B. de Almeida, P.S. Prata, M.A. Zaghete, et al., CeO2 Nanoparticle Morphologies and Their Corresponding Crystalline Planes for the Photocatalytic Degradation of Organic Pollutants, ACS Applied Nano Materials 2 (2019) 6513–6526, https://doi.org/10.1021/acsanm.9b01452.

[15] Z. Fan, F. Meng, J. Gong, H. Li, Y. Hu, D. Liu, Enhanced photocatalytic activity of hierarchical flower-like CeO2/TiO2 heterostructures, Mater. Lett. 175 (2016) 36–39, https://doi.org/10.1016/j.matlet.2016.03.136.

[16] Y. Kim, C. Hwang, I. Kim, J. Kim, B. Ryu, Effects of heat treatment on morphology and crystallization of glass and film containing a large amount of CdO, Electron. Mater. Lett. 10 (2014) 1163–1169, https://doi.org/10.1007/s13391-014-4112-8.

[17] E. Amaterz, A. Bouddouch, A. Chennah, A. Tara, A. Taoufyq, B. Bakiz, et al., Heat treatment effect on the structure and morphology of strontium monoacid orthophosphate thin films, Mater. Today:. Proc. 22 (2020) 45–47, https://doi.org/10.1016/j.matpr.2019.08.070.

[18] K. Ackland, J.M.D. Coey, Room temperature magnetism in CeO2—A review, Phys. Rep. 746 (2018) 1–39, https://doi.org/10.1016/j.physrep.2018.04.002.

[19] R.N. Blumenthal, R.K. Sharma, Electronic conductivity in nonstoichiometric cerium dioxide, J. Solid State Chem. 13 (1975) 360–364, https://doi.org/10.1016/0022-4596(75)90152-8.

[20] R.N. Blumenthal, R.L. Hofmaier, The Temperature and Compositional Dependence of the Electrical Conductivity of Nonstoichiometric CeO[sub 2−x], J. Electrochem. Soc. 121 (1974) 126, https://doi.org/10.1149/1.2396805.

[21] P. Wang, F. Meng, C. Gao, W. Xie, J. Wang, A. Li, Structural, morphological and optical characteristics of fusiform Co-doped CeO2 via a facile hydrothermal method, J. Mater. Sci.: Mater. Electron. 2018;29. https://doi.org/10.1007/s10854-018-9243-5.

[22] G.P. Casali, T. Mazzo, E. Longo, R. Muccillo, Síntese e propriedades fotoluminescentes do óxido de cério dopado com magnésio, Cerâmica 60 (2014) 371–378, https://doi.org/10.1590/s0366-69132014000300008.

[23] X. Yang, Y. Liu, J. Li, Y. Zhang, Effects of calcination temperature on morphology and structure of CeO2 nanofibers and their photocatalytic activity, Mater. Lett. 241 (2019) 76–79, https://doi.org/10.1016/j.matlet.2019.01.006.

[24] A. Arabacı, Effect of the calcination temperature on the properties of Sm-doped CeO2, Emerging Mater. Res. 9 (2020) 296–301, https://doi.org/10.1680/jemmr.18.00082.

[25] J.D.C. Carregosa, J.P.F. Grilo, G.S. Godoi, D.A. Macedo, R.M. Nascimento, R.M.P.B. Oliveira, Microwave-assisted hydrothermal synthesis of ceria (CeO2): Microstructure, sinterability and electrical properties, Ceram. Int. 46 (2020) 23271–23275, https://doi.org/10.1016/j.ceramint.2020.06.021.

[26] S. Maya-Johnson, L. Gracia, E. Longo, J. Andres, E.R. Leite, Synthesis of cuboctahedral CeO2 nanoclusters and their assembly into cuboid nanoparticles by oriented attachment, ChemNanoMat 3 (2017) 228–232, https://doi.org/10.1002/cnma.201700005.

[27] J. Andrés, L. Gracia, A.F. Gouveia, M.M. Ferrer, E. Longo, Effects of surface stability on the morphological transformation of metals and metal oxides as investigated by first-principles calculations, Nanotechnology 26 (2015), 405703, https://doi.org/10.1088/0957-4484/26/40/405703.

[28] F. Meng, L. Wang, J. Cui, Controllable synthesis and optical properties of nano-CeO2 via a facile hydrothermal route, J. Alloy. Compd. 556 (2013) 102–108, https://doi.org/10.1016/j.jallcom.2012.12.096.

[29] O.E. Everett Espino, P.C. Zonetti, R.R. Celin, L.T. Costa, O.C. Alves, J.C. Spadotto, et al., The tendency of supports to generate oxygen vacancies and the catalytic performance of Ni/ZrO2 and Ni/Mg(Al)O in CO2 methanation, Cat. Sci. Technol. 12 (2022) 1324–1338, https://doi.org/10.1039/D1CY01915E.

[30] L. Yang, Y. Yu, H. He, Y. Zhang, X. Qin, B. Wang, Oxygen vacancy clusters essential for the catalytic activity of CeO2 nanocubes for o-xylene oxidation, Sci. Rep. 7 (2017) 12845, https://doi.org/10.1038/s41598-017-13178-6.

[31] J. Li, Z. Jiang, K. Qian, W. Huang, Effect of Calcination Temperature on Surface Oxygen Vacancies and Catalytic Performance Towards CO Oxidation of Co₃O₄ Nanoparticles Supported on SiO2, Chin. J. Chem. Phys. 25 (2012) 103–109, https://doi.org/10.1088/1674-0068/25/01/103-109.

[32] S. Tiwari, G. Rathore, N. Patra, A.K. Yadav, D. Bhattacharya, S.N. Jha, et al., Oxygen and cerium defects mediated changes in structural, optical and photoluminescence properties of Ni substituted CeO2, J. Alloy. Compd. 782 (2019) 689–698, https://doi.org/10.1016/j.jallcom.2018.12.009.

[33] M. Lekgoathi, L. Kock, Effect of short and long range order on crystal structure interpretation: Raman and powder X-ray diffraction of LiPF6. Spectrochimica Acta

Part A: Mol. Biomol. Spectrosc., 2015;153. https://doi.org/10.1016/j.saa.2015.09.025.

[34] S. Phokha, S. Pinitsoontorn, P. Chirawatkul, Y. Poo-arporn, S. Maensiri, Synthesis, characterization, and magnetic properties of monodisperse CeO2 nanospheres prepared by PVP-assisted hydrothermal method, Nanoscale Res. Lett. 7 (2012) 425, https://doi.org/10.1186/1556-276X-7-425.

[35] N. Sangiorgi, L. Aversa, R. Tatti, R. Verucchi, A. Sanson, Spectrophotometric method for optical band gap and electronic transitions determination of semiconductor materials, Opt. Mater. 64 (2017) 18–25, https://doi.org/10.1016/j.optmat.2016.11.014.

[36] D.L. Wood, J. Tauc, Weak Absorption Tails in Amorphous Semiconductors, Phys. Rev. B 5 (1972) 3144–3151, https://doi.org/10.1103/PhysRevB.5.3144.

[37] M.D.P. Silva, R.F. Gonçalves, I.C. Nogueira, V.M. Longo, L. Mondoni, M.G. Moron, et al., Microwave-assisted hydrothermal synthesis of Ag2(W1-xMox)O4 heterostructures: Nucleation of Ag, morphology, and photoluminescence properties, Spectrochim. Acta A Mol. Biomol. Spectrosc. 153 (2016) 428–435, https://doi.org/10.1016/j.saa.2015.08.047.

[38] A. Abd-Elnaiem, A. Hakamy, I. Ibrahem, A. Ali, W. Mohamed, Z.E. Abo, Thermal-induced effects on the structural and photocatalytic properties of nickel oxide nanoparticles for indigo carmine dye removal, J. Inorg. Organometallic Polym. Mater. (2022), https://doi.org/10.1007/s10904-022-02277-1.

[39] A.B. Sifontes, M. Rosales, F.J. Méndez, O. Oviedo, T. Zoltan, Effect of calcination temperature on structural properties and photocatalytic activity of ceria nanoparticles synthesized employing chitosan as template, J. Nanomater., 2013; 2013. https://doi.org/10.1155/2013/265797.

[40] L. Wang, F. Meng, K. Li, F. Lu, Characterization and optical properties of pole-like nano-CeO2 synthesized by a facile hydrothermal method, Appl. Surf. Sci. 286 (2013) 269–274, https://doi.org/10.1016/j.apsusc.2013.09.067.

[41] R.A. Ciola Amoresi, R. Cristina de Oliveira, L. Cichetto, P.M. Desimone, C.M. Aldao, M.A. Ponce, et al. Pure and Ni2O3-decorated CeO2 nanoparticles applied as CO gas sensor: Experimental and theoretical insights, Ceram. Int., 2022;48: 14014–25. https://doi.org/10.1016/j.ceramint.2022.01.286.

[42] N. Yamazoe, K. Suematsu, K. Shimanoe, Extension of receptor function theory to include two types of adsorbed oxygen for oxide semiconductor gas sensors, Sens. Actuators B 163 (2012) 128–135, https://doi.org/10.1016/j.snb.2012.01.020.

[43] L. Wang, F. Meng, Oxygen vacancy and Ce3+ ion dependent magnetism of monocrystal CeO2 nanopoles synthesized by a facile hydrothermal method, Mater. Res. Bull. 48 (2013) 3492–3498, https://doi.org/10.1016/j.materresbull.2013.05.036.